Distribution of Alloying Quadrivalent Zirconium in TiO2-x Magnèli Phase

Teramoto, Takeshi
Takai, Yutaka
Hashiguchi, Hiroki
Okunishi, Eiji
Tanaka, Katsushi

(Citation)
Materials Transactions,60(10):2199-2203

(Issue Date)
2019-10-01

(Resource Type)
journal article

(Version)
Version of Record

Materials Transactions, Vol. 60, No. 10 (2019) pp. 2199 to 2203

Distribution of Alloying Quadrivalent Zirconium in TiO_{2-x} Magnèli Phase

Takeshi Teramoto[1,*1], Yutaka Takai[1,*2], Hiroki Hashiguchi[2], Eiji Okunishi[2] and Katsushi Tanaka[1]

[1]*Department of Mechanical Engineering, Kobe University, Kobe 657-8501, Japan*
[2]*JEOL, Ltd., Tokyo 196-8558, Japan*

The alloying effect of ZrO_2 on the microstructure of the thermoelectric material, Ti_nO_{2n-1}, which is a partially reduced rutile phase called the Magnèli phase, is investigated. The microstructure of Ti_nO_{2n-1} is characterized by periodically induced planar defects, called shear planes, in the rutile matrix. The configuration of the O atoms around a Ti atom in a shear plane is different from that in the rutile matrix but similar to that in Ti_2O_3. It is speculated that the alloying of ZrO_2, which has an equivalent structure to that of rutile, causes preferential Zr addition in the rutile matrix. From the microstructural observation of the alloying specimen ($Ti_{10}O_{19}$+6 mol%ZrO_2), it is revealed that the added Zr is distributed homogeneously in the entire microstructure because the valence of the Ti atoms in the matrix rutile and shear plane is similar.
[doi:10.2320/matertrans.MT-M2019155]

(Received May 31, 2019; Accepted July 16, 2019; Published August 30, 2019)

Keywords: *Magnèli phase, STEM-EELS, titanium oxide*

1. Introduction

The crystal structures of the partially reduced rutile homologous series known as Magnèli phases[1] are expressed as $Ti_nO_{2n-1}(TiO_{2-x})$, which are characterized as the so-called crystallographic shear structures.[2] Such a crystal structure is an atomistic scale lamellar structure consisting of monolayers with a chemical composition of Ti_2O_3 regularly embedded in the TiO_2 matrix[3] as schematically illustrated in Fig. 1. Notably, the vacancies are not introduced at the oxygen sites, instead interstitial Ti atoms and an associated rearrangement of Ti atoms are found by the reduction of TiO_2. Because electric conduction is improved by reduction, TiO_{2-x} is used as an oxide-based electrode.[4]

Some researchers have reported[5–7] that partially reduced rutile exhibits a relatively good thermoelectric property. Harada *et al.*[8] have reported that the regularly embedded planar defects significantly reduce the lattice thermal conductivity, and a maximum dimensionless figure of merit ZT of 0.03 is obtained for $TiO_{1.9}$ at 700 K. If a further reduction in the lattice thermal conductivity is realized by alloying elements, an improvement in the thermoelectric property is expected. However, as many researchers have indicated, the effects of an alloying element reduce not only the lattice thermal conductivity but also the electric conductivity in general.

From the viewpoint of the crystal structure of the Magnèli phase of TiO_{2-x}, a segregation of the alloying element is expected, i.e., trivalent and quadrivalent elements preferentially substitute Ti atoms in the atomic layers having chemical compositions of Ti_2O_3 and TiO_2, respectively. If the electric conduction of TiO_{2-x} originates from the layers having the chemical composition of Ti_2O_3 and quadrivalent alloying elements preferentially segregate in the TiO_2 layers, then the quadrivalent alloying elements reduce the lattice thermal conductivity without significantly reducing the electric conductivity. The degree of the segregation of the trivalent and quadrivalent elements may be governed by the valence state of the Ti atoms in the layers having chemical compositions of Ti_2O_3 and TiO_2. There are some studies[9–13] in which the valence state of the Ti atoms in the Magnèli phase was examined. Lakkis *et al.*[13] have reported that the valence states of all the Ti atoms in Ti_4O_7 ($TiO_{1.75}$) are +3.5 at high temperatures ($T > 150$ K); however, the local composition is different in each layer. Below 130 K, the charges are localized to form Ti^{+3}–Ti^{+3} and Ti^{+4}–Ti^{+4} chains. This valence state transition is closely related to the electrical conduction, such that the conductivity increases by two or three orders from a low- to high-temperature state. However, the valence state transition is not observed for crystals with a small degree of reduction, e.g., $Ti_9O_{17}(TiO_{1.88})$.[14] This may be because the crystallographic shear plane is widely separated in such less reduced crystals. This implies that the difference in the local chemical composition has a strong effect on the valence state in a less reduced rutile. In this report, the distribution of quadrivalent Zr in $TiO_{1.9}$ and valence state of Ti are investigated.

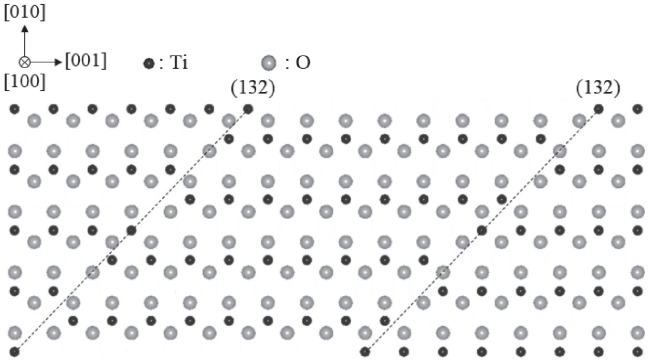

Fig. 1 Schematic of the shear microstructure of Ti_nO_{2n-1}.

2. Experimental and Analysis Procedure

2.1 Microstructural observation

The powders of $(Ti_{0.94}, Zr_{0.06})O_{1.906}$ were synthesized from an appropriate mixture of TiO_2, TiO, and ZrO_2 powders.

*1Corresponding author, E-mail: teramoto@mech.kobe-u.ac.jp
*2Graduate Student, Kobe University. Present address: Kawasaki Heavy Industries, Ltd., Tokyo 105-8315, Japan

According to the reported phase diagram of a TiO_2–ZrO_2 system,[15] this composition is expected in a solid solution at 1473 K if the phase diagram is not affected by the reduction. The powders were suspended in ethanol and mixed by a planetary ball mill at 360 rpm for 3 h in a ZrO_2 pot and milling balls. The slurry obtained was dried and cold pressed to form a pellet, which was followed by sintering in vacuum at 1473 K for 24 h. The pellet was hot pressed in a graphite cylinder at 1473 K for 10 min under a compressive stress of 50 MPa. To examine the synthesized phase, X-ray diffraction analysis was conducted. Small plates were cut from the pellet and thinned by using an ion slicer. The foil was examined using scanning transmission electron microscopy (STEM) together with energy dispersion X-ray spectroscopy (EDX) and electron energy loss spectroscopy (EELS).

2.2 Evaluation of valence state of Ti ions

The EELS spectra consist of $L_{2,3}$ and *O-K* edges. The $L_{2,3}$ edge of Ti_nO_{2n-1} consists of four peaks corresponding to different the transitions of electrons.[16–18] To evaluate the valence state of the Ti ions, a quantification technique[18] based on the chemical shift of the Ti-$L_{2,3}$ spectra was performed. In this method, the valence state of Ti ions is quantified using the integrated intensity ratio of L_2 and L_3 peaks. Integration windows with a width of 1 eV are applied to obtain the integrated intensities of the L_2 and L_3 peaks. Stoyanov *et al.* proposed the following equation to quantify the concentration of Ti^{4+} ions from the ratio of the integrated intensities:

$$x = \ln((\mathrm{I}(L_2)/\mathrm{I}(L_3) - 0.87953)/0.21992) \times 0.21767 \quad (1)$$

where x is the concentration of Ti^{4+} ions and $I(L_2)$ and $I(L_3)$ are the integrated intensities of the L_2 and L_3 peaks, respectively.

3. Results

3.1 Phase and microstructure identification

Figure 2 shows the X-ray diffraction profiles obtained from the present specimen and those from $TiO_{1.90}$, TiO_2,[19] and ZrO_2.[20] No trace of peaks resulting from the residual phases of TiO_2 and ZrO_2 is observed, and the profile practically agrees with that of $TiO_{1.90}$. This indicates that the Zr is a solid solution in the Magnèli phase under the present heat treatment. Alloying with Zr causes a small peak shift toward a small diffracted angle owing to the size of a Zr^{+4} ion being larger than that of a Ti^{+4} ion. It is reported that the profile is systemically changed by the degree of reduction.[1] From the width of the peak separation caused by the periodic crystallographic shear structure, the present specimen is evaluated as $(Ti_{0.94}, Zr_{0.06})O_{1.906}$.

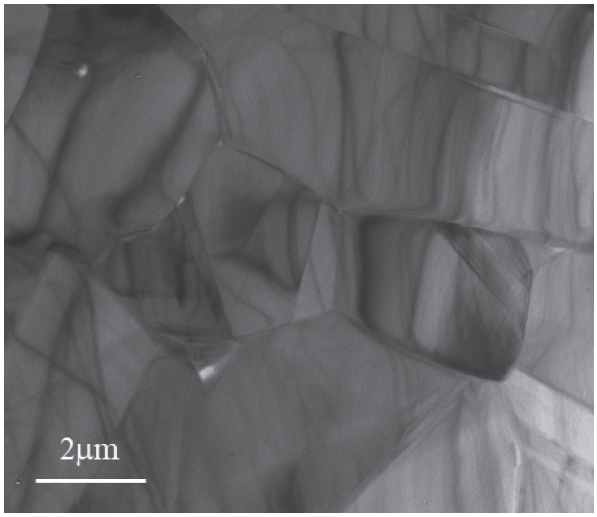

Fig. 3 Low-magnification TEM bright-field image.

Figure 3 shows a low-magnification TEM bright-field image. Similar to the above X-ray diffraction analysis, no trace of a secondary phase is observed. From this image, the mean grain size is estimated as 2.9 μm. Figure 4(a) shows a high angle annular dark field (HAADF) image captured from the $[1\bar{1}1]$ crystallographic direction, where a Ti atom column is observed as a bright contrast. In this image, a periodic planar defect corresponding to a crystallographic shear plane is clearly observed. Figure 4(b) shows the selected area electron diffraction (SAED) pattern obtained from the same grain in Fig. 4(a). Superlattice reflections caused by the periodic crystallographic shear plane are observed, and the reflection spots are approximately aligned along the 132 diffraction spot of the underlying rutile crystal. Because the interval of the superlattice reflection spots is about 14 times the (132) interplanar spacing of the underlying rutile crystal, the average composition of this grain is estimated to be approximately $(Ti, Zr)_{14}O_{27}$ $(= (Ti, Zr)O_{1.93})$, which is in agreement with the result of

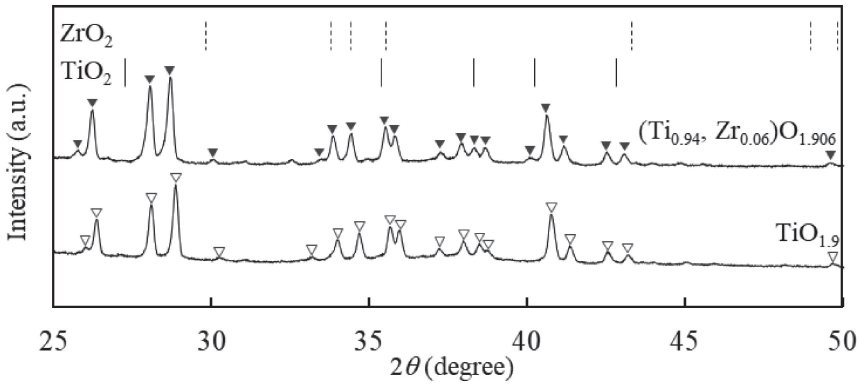

Fig. 2 XRD patterns of $TiO_{1.9}$, $(Ti_{0.94}, Zr_{0.06})O_{1.9}$, TiO_2,[19] and ZrO_2.[20]

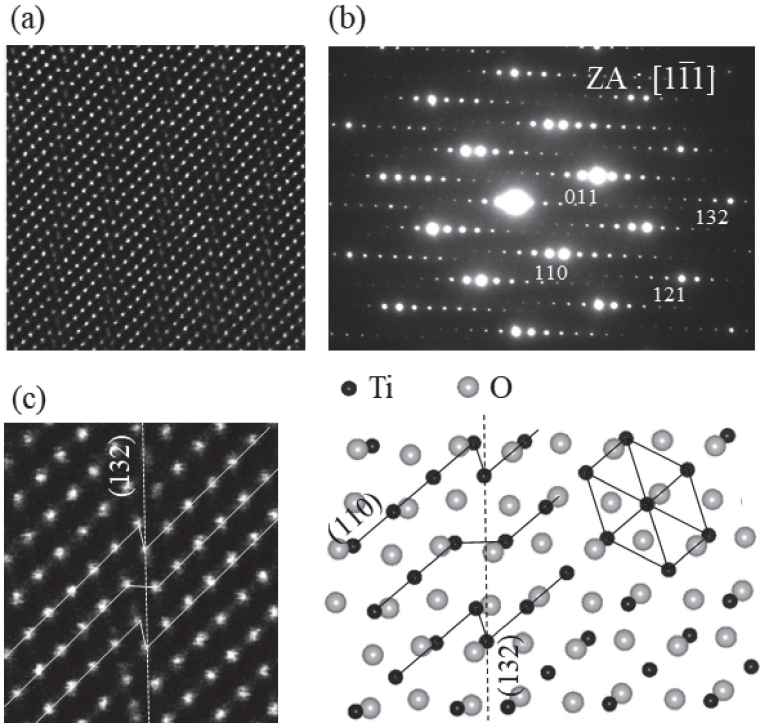

Fig. 4 (a) HAADF-STEM image along the [1$\bar{1}$1] zone axis, (b) SAED pattern, (c) Highly magnified image and model of the shear plane.

the X-ray diffraction analysis. Figure 4(c) shows a highly magnified image near the shear plane and schematic image of the shear structure. The (110) column across the shear plane is represented as lines. In the crystallographic shear plane, the arrangement of the Ti atom columns is shifted leading to a local composition of Ti_2O_3.

3.2 Distribution of Zr

Figure 5(a)–(d) show the result of the STEM-EDS analysis. Figure 5(a) shows the HAADF image of the shear microstructure. Figure 5(b) shows the schematic of the Ti atom arrangement and shear microstructure in the HAADF image. The grayed area in this figure indicates the positions of the shear planes. The curvature of the shear planes is caused by a local fluctuation of the reduction ratio. Figure 5(c) and (d) exhibit the distributions of Ti and Zr elements, respectively. If Zr atoms are segregated in the TiO_2 matrix, then relatively dark bands should be observed at the positions of the shear planes in Fig. 5(d). However, the observed distribution of the Zr atoms is homogeneous, indicating that the Zr atoms are not segregated in the TiO_2 matrix.

Figure 6(a) again shows the HAADF image of the shear microstructure. During the acquisition of this HAADF image, the EELS spectrum at each point is also recorded. The EELS spectra obtained at the points in areas A and B are integrated to yield spectra with a better signal to noise ratio from the Ti atoms on the crystallographic shear planes and in the TiO_2 matrix, respectively. Figure 6(b) shows the spectra with the energy loss corresponding to the Ti-$L_{2,3}$ edge obtained from areas A and B, respectively, together with the spectra obtained for TiO_2 and Ti_2O_3.[17] The EELS spectra obtained from areas A and B are slightly different and have a different shape compared to those obtained for TiO_2 and Ti_2O_3. This indicates that the valence states of the Ti atoms on the crystallographic shear plane are different from those of the Ti atoms in the matrix, TiO_2, and Ti_2O_3.

4. Discussion

Although a segregation of Zr atoms in the TiO_2 matrix is expected when the local crystallographic environment is considered, a homogeneous distribution of Zr atoms is observed, as shown in Fig. 5. This suggests that the valence state of the Ti ions on the crystallographic shear planes is the same as of those in the TiO_2 matrix. To clarify the valence state of the Ti ions on the crystallographic shear planes and in the TiO_2 matrix, a quantitative analysis of the EELS spectra is performed as follows.

The EELS spectra of the Ti-$L_{2,3}$ edge exhibits four peaks (*a*, *b*, *c*, and *d*). The peaks of *a*, *b* and *c*, *d* in Fig. 6(b) correspond to the L_3 and L_2 edges, respectively. The valence state of the Ti ions is quantified using the integrated intensity, which is obtained from an integration window of 1 eV width, as the ratio of the L_2 and L_3 peaks. The positions of the integration windows are shown in Fig. 6(b) as dotted lines. One of the integration windows is set from 465.5 to 466.5, corresponding to the first peak in the L_3 region (peak *a*) of the spectrum of Ti_2O_3. The other is set from 456.2 to 457.2 eV, corresponding to the second L_2 peak in the L_2 region (peak *d*) of the spectrum of TiO_2. From eq. (1), the valence state of the Ti ions on the crystallographic shear plane and in the TiO_2 matrix is 3.78 and 3.84, respectively. When the volume ratio of the region of the crystallographic shear planes is considered, the valence state of the Ti ions averaged for the entire crystal is estimated as 3.83. Because the actual composition of this specimen is $Ti(Zr)O_{1.93}$ as mentioned above, for this composition, the average valence

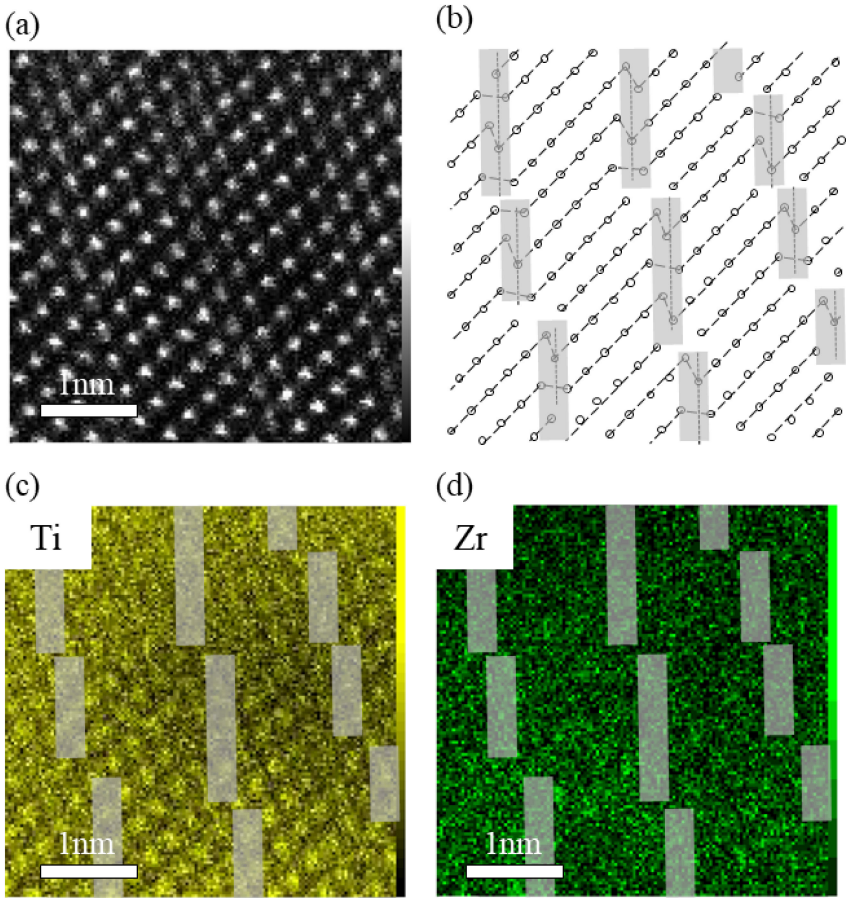

Fig. 5 EDS mapping images (a) HAADF-STEM image (b) Schematic of the Ti atom arrangement and shear microstructure in the HAADF-STEM image (c, d) Mapping images of Ti and Zr (grayed area corresponds to the shear plane).

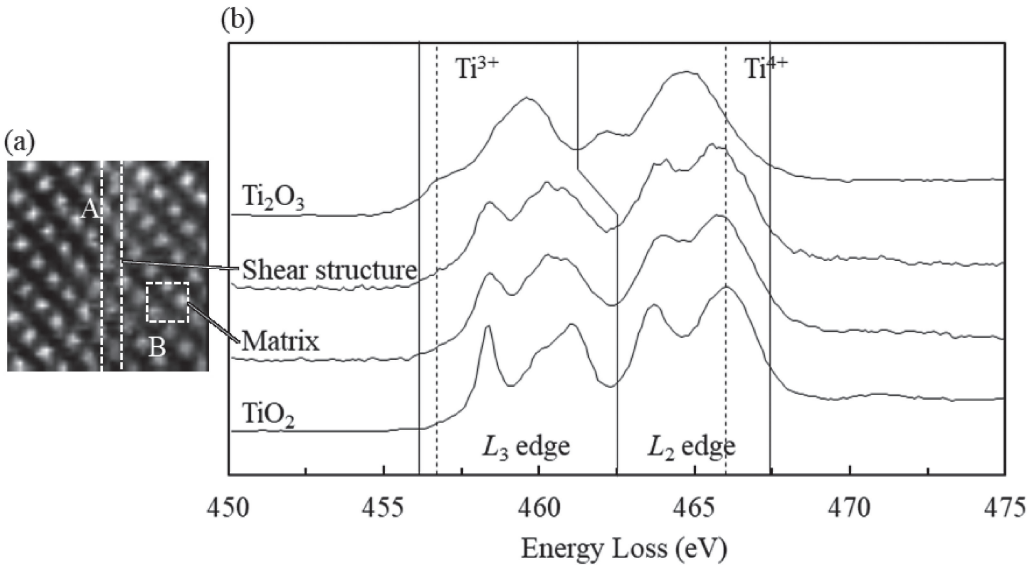

Fig. 6 STEM-EELS analysis (a) Acquisition point of the EELS-spectrum (b) Ti-$L_{2,3}$ edge of the EELS spectrum.

states of the transition metals are calculated as 3.86, in good agreement with the present analysis.

When the valence states of Ti ions are governed by the local crystallographic environments, the values are expected to be +3 for the Ti ions on the crystallographic shear structure and +4 for the Ti ions in the TiO_2 matrix, respectively. In the actual microstructure, however, the interactions of the valence states are remarkable, and the distribution of the valence states of the Ti ions is practically homogeneous over the entire crystal having a crystallographic shear structure. Owing to the homogeneity of the valence states of the Ti ions, the quadrivalent Zr ions distribute homogeneously over the entire crystal having a crystallographic shear structure.

It is assumed that Zr ions distributed over the entire microstructure become the scattering source of the carrier and the phonon, and reduce the electrical conductivity and the lattice thermal conductivity. It is difficult to control the electrical conductivity and lattice thermal conductivity independently by the segregation of the Zr based on the valence states distribution on the microstructure.

5. Conclusions

The distributions of alloying quadrivalent Zr and of the valence states of the Ti ions in $(Ti_{0.94}, Zr_{0.06})O_{1.9}$ have been investigated via STEM-EDS and STEM-EELS analyses. The findings are summarized as follows:

(1) Zr ions substitute the Ti ions in $TiO_{1.9}$ on alloying. The formation of the crystallographic shear structure is not affected by the substitution.
(2) Quadrivalent Zr ions distribute homogeneously over the entire crystal having the crystallographic shear structure regardless of the differences in the local crystallographic environment.
(3) The valence states of the Ti ions on the crystallographic shear structure and in the TiO_2 matrix are determined as 3.78 and 3.84, respectively. This nearly homogeneous valence distribution is the reason Zr atoms distribute homogeneously.

Acknowledgements

This work was supported by the Grants-in-Aid for Scientific Research (Grant Number 18H01737) from the Japan Society for the Promotion of Science.

REFERENCES

1) S. Andersson, B. Collén, U. Kuylenstierna and A. Magnéli: Acta Chem. Scand. **11** (1957) 1641–1652.
2) J.S. Anderson and B.G. Hyde: J. Phys. Chem. Solids **28** (1967) 1393–1408.
3) L.A. Bursill and B.G. Hyde: Prog. Solid State Chem. **7** (1972) 177–253.
4) R.F. Bartholomew and D.R. Frankl: Phys. Rev. **187** (1969) 828–833.
5) Y. Lu, M. Hirohashi and K. Sato: Mater. Trans. **47** (2006) 1449–1452.
6) W.R. Thurber and A.J.H. Mante: Phys. Rev. **139** (1965) A1655–A1665.
7) Y. Lu, Y. Matsuda, K. Sagara, L. Hao, T. Otomitsu and H. Yoshida: Adv. Mater. Res. **415–417** (2011) 1291–1296.
8) S. Harada, K. Tanaka and H. Inui: J. Appl. Phys. **108** (2010) 083703.
9) M. Marezio, D.B. McWhan, J.P. Remeika and P.D. Dernier: Phys. Rev. B **5** (1972) 2541–2551.
10) Y.L.E. Page and M. Marezio: Recherche **3** (1984) 13–21.
11) L. Liborio, G. Mallia and N. Harrison: Phys. Rev. B **79** (2009) 245133.
12) J.S. Anderson and A.S. Khan: J. Less-Common Met. **22** (1970) 219–223.
13) S. Lakkis, C. Schlenker, B. Chakraverty and R. Buder: Phys. Rev. B **14** (1976) 1429–1440.
14) A.D. Inglis, C.M. Hurd and P. Strobel: J. Phys. C **17** (1984) 6801–6809.
15) U. Troitzsch and D.J. Ellis: J. Mater. Sci. **40** (2005) 4571–4577.
16) V. Eyert, U. Schwingenschlögl and U. Eckern: Chem. Phys. Lett. **390** (2004) 151–156.
17) M. Tian, M. Mahjouri-Samani, G. Eres, R. Sachan, M. Yoon, M.F. Chisholm, K. Wang, A.A. Puretzky, C.M. Rouleau, D.B. Geohegan and G. Duscher: ACS Nano **9** (2015) 10482–10488.
18) E. Stoyanov, F. Langenhorst and G. Steinle-Neumann: Am. Mineral. **92** (2007) 577–586.
19) R.J. Swope, J.R. Smyth and A.C. Larson: Am. Mineral. **80** (1995) 448–453.
20) C.J. Howard, E.H. Kisi, R.B. Roberts and R.J. Hill: J. Am. Ceram. Soc. **73** (1990) 2828–2833.